

Room and Low-Temperature Performance for a Sub-Attifarad Capacitance Sensor for Precision Measurements, Including Applications in Gravitational Wave Detectors

S. Saraf, C.Y. Lui, S. Wang, S. Buchman, J. Lipa

¹*SN&N Electronics, Inc., 1846 Stone Avenue, San Jose, CA 95125 USA*

²*Hainan Tropical Ocean University, Sanya, 572022 China*

³*Hansen Experimental Physics Laboratory, Stanford, CA 95038 USA*

Abstract

We describe the design principles, fabrication, and characterization of a precision AC capacitance sensor with a measured $0.33 \text{ aF}/\sqrt{\text{Hz}}$ short term sensitivity, at 118 kHz bridge resonance frequency and at 1 Hz Fourier measurement frequency. The sensor is based on a high-Q resonant differential planar printed circuit board transformer that provides an excellent improvement in signal-to-noise of over two orders of magnitude, compared with a standard transformer-based capacitance bridge. Cryogenic operation of the transformer at 120 K resulted in a measured sensitivity of $0.21 \text{ aF}/\sqrt{\text{Hz}}$ at 1 Hz, which, extrapolated to 3 K, would yield a capacitance sensitivity $\sim 0.03 \text{ aF}/\sqrt{\text{Hz}}$. Repeating the experiment with a second transformer core yielded sensitivities of $0.42 \text{ aF}/\sqrt{\text{Hz}}$ and $0.34 \text{ aF}/\sqrt{\text{Hz}}$ at 293 K and 125 K respectively, providing a first order approximation of the variability of the sensor performance. 28-hours room temperature runs with the two cores demonstrated long-term sensitivities of $0.36 \pm 0.01 \text{ aF}/\sqrt{\text{Hz}}$ and $0.46 \pm 0.01 \text{ aF}/\sqrt{\text{Hz}}$ respectively.

I. INTRODUCTION

There are several applications that require precise and stable measurements of capacitances with resolution at the attofarad level. Accurate proximity sensing relies on capacitance measurements for applications like microscope focusing, lens alignment or stress analysis¹. Scanning capacitance microscopy employs capacitance measurements to raster scan a probe to get an image of surface topography or local changes of dielectric constant². Position sensors that infer a relative sub-nm displacement via a capacitance measurement have important applications in many space-based relativity experiments like Gravity Probe B³ and tests of the equivalence principle^{4,5}. Space-based gravitational wave antennas like the LISA⁶, Taiji⁷, and TianQin⁸ missions employ capacitance-based position sensors in conjunction with high voltage actuation systems for drag-free operation of a gravitational reference sensor as part of a disturbance reduction system⁹.

As is common practice, the instrument described here is based on an AC capacitance bridge with the advantage of performing a high signal-to-noise measurement that is not at DC. Since the drive frequency of the bridge is known, resonant operation with stable inductors or transformers will improve the signal-to-noise of the measurement. There are several advantages to using a resonant differential transformer. First, the signal-to-noise ratio is enhanced by the quality factor Q of the resonant circuit at the operating frequency. Second, common-mode noise is nulled out to first order due to the differential operation of the transformer's primary windings. Third, due to transformer action, there is electrical isolation of the front-end electronics from the sensing electronics. This prevents formation of ground loops, while balanced differential operation will reduce other forms of coupling to the precision measurement system.

To date, the state-of-the-art in capacitance sensing for a similar application was demonstrated by the LISA Pathfinder (LPF) mission¹⁰, showing a noise performance of between 0.7 aF/ $\sqrt{\text{Hz}}$ and 1.8 aF/ $\sqrt{\text{Hz}}$ (for an excitation voltage of 0.6 V) down to a frequency of 1 mHz. Measurements showed¹⁰ a 2.6 spread factor between the noise figures of the 12 nominally identical bridges; two for each of the three axes of the two test masses. This spread was traced to hard to control variations of property details in the hardware. It must be emphasized that this performance was achieved as part of a complete system that included the higher voltages of the forcing function for the test masses, as well as all other noise sources contributed by the auxiliary electronics and hardware.

The hardware development, implementation, and testing of the capacitance bridge presented in this work was performed by SN&N Electronics¹¹ in collaboration with Stanford University and funded through the Changchun Institute of Optics, Fine Mechanics and Physics (CIOMP) of the Chinese Academy of Science, as described in detail in a number of technical reports^{12,13,14}. A test by CIOMP, using the design detailed in the aforementioned technical reports¹⁵, resulted in a noise level of 1.1 aF/ $\sqrt{\text{Hz}}$ for frequencies of between 10 mHz and 1 Hz. Our calculations for, and actual results of tests with the SN&N hardware, are presented in this paper and show a three-times better performance than those in reference 15.

Simulations and analyses of the practical limits for scanning capacitance microscopy² predict a sensitivity of 0.36 aF in a 1 kHz bandwidth measurement. However, this limit is derived by constraints due to the geometry of the scanning tip rather than by the capacitance bridge electronics. For the top performing commercially available capacitance meters see the Andeen-Hagerling instruments¹⁶.

Table 1 shows the performance of capacitance bridges in applications similar to the one described here. The first row refers to the instruments flown on the geodesy missions GRACE¹⁷, GRACE-FO¹⁸, and GOCE¹⁹ and on the equivalence principle measurement MICROSCOPE²⁰; all developed by CNES, the French National Centre for Space Studies. Note that the capacitance to

the test masses is significantly larger in these instruments, compared to the gravitational wave detectors test masses of LISA Pathfinder²¹, TianQin⁸, and Taiji⁷ represented in all other rows and developed by the European Space Agency (ESA), the Huazhong University of Science in China, and SN&N Electronics respectively.

Table 1. Performance of capacitance sensors for applications similar to the one described in this paper

Application	Instrument Design and Manufacture	Resonant Frequency (kHz)	Capacitance Resolution (aF/ $\sqrt{\text{Hz}}$) \times V	Capacitance Resolution (aF/ $\sqrt{\text{Hz}}$) \times V \times (f/100kHz) ^{3/2}	Comments
GRACE, GRACE-FO, GOCE, MICROSCOPE	CNES	100	0.7 ^{22,23}	0.7	Complete flight systems
LISA Pathfinder	ESA	100	0.4 - 1.1 ¹⁰	0.4 - 1.1	Complete flight systems
TianQin	Huazhong U. of Science, China	50	1.2 ²⁴	0.4	Laboratory Capacitance Bridge
TianQin	Huazhong U. of Science, China	200	0.7 ²⁵	2.0	Laboratory Capacitance Bridge
Precision Meas. and GW detection THIS WORK CORE#1	SN&N, USA	118	0.33 - 0.21 [†]	0.36 - 0.23 [†]	Laboratory Capacitance Bridge
Precision Meas. and GW detection THIS WORK CORE#2	SN&N, USA	118	0.42 - 0.34 [†]	0.46 - 0.37 [†]	Laboratory Capacitance Bridge

The capacitance resolutions given in column four are normalized to an excitation level of 1 V, while those in column five are further scaled with the 3/2 power of the resonant frequency.

II. RESONANT TRANSFORMER DESIGN

Figure 1 shows a schematic of the resonant capacitance bridge (RCB) with the transformer primaries configured in differential operation. I_{p1} and I_{p2} are the primary currents, and the identical transformer primary windings are configured such that the flux in the common core will cancel out when the bridge is in balance. The resonant frequency of the tuned bridge is given by:

$$f_0 = \frac{1}{2\pi\sqrt{LC_{eq}}} \quad (1)$$

where $C_{eq} = C_1 + C_2 + C_{p1} + C_{p2}$ and $L = L_1 = L_2$ is the inductance of the primary windings. For the nominal case, where the capacitances to the test mass and the tuning capacitances are equal,

[†] Measured in this work with the transformer of the SN&N capacitance bridge at ~123 K

$C_1 = C_2 = C_0$ and $C_{p1} = C_{p2} = C_p$, the equivalent capacitance for resonant operation is given by: $C_{eq} = 2(C_0 + C_p)$.

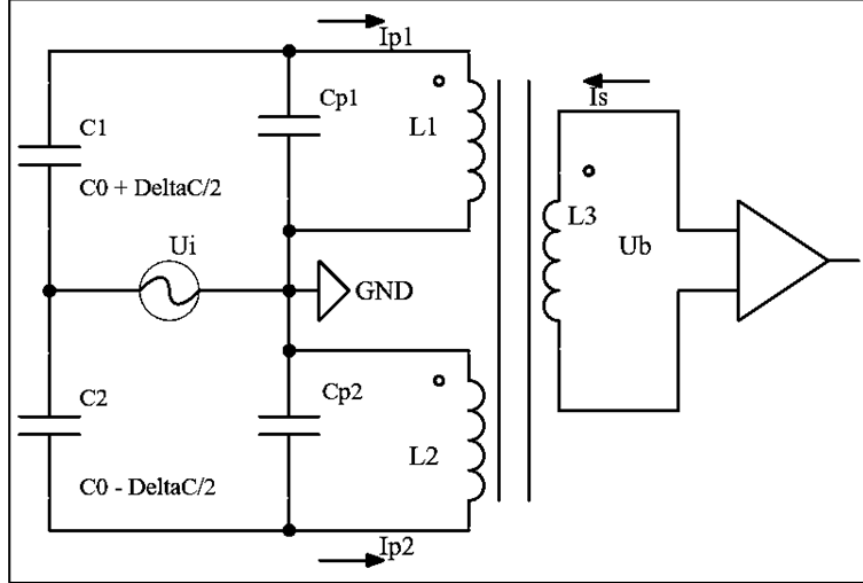


Figure 1. Simplified diagram of a resonant capacitive bridge for noise calculations. C_{p1} and C_{p2} are the fixed capacitors in the bridge and serve as tuning capacitors for the resonant transformer primaries. C_1 and C_2 represent the capacitances to the test mass.

Circuit analysis of the bridge architecture yields the following equation for the magnitude of the bridge output voltage U_b at resonance frequency f_0

$$|U_b(f_0)| = \frac{Q}{C_{eq}} \Delta C U_i \quad (2)$$

where Q is the quality factor of the bridge, ΔC is the differential capacitance between the two arms of the bridge (where for $\Delta C \ll C_{1,2}$, $\Delta C_{1,2} = \pm \Delta C/2$), and U_i is the bridge actuation voltage, typically $\sim 1V$. Synchronous demodulation would follow the AC amplifier stages to extract the differential capacitance at low frequencies for further analog and digital processing. The demodulation aspects of the detector are not discussed in this paper, except to note that synchronous demodulation has a $\sqrt{2}$ noise penalty associated with it from the RF mixing process. The equivalent capacitance noise limited by the bridge thermal noise can be written as:

$$S_C^{1/2} = \frac{1}{U_i} * \sqrt{\frac{8k_B T}{(2\pi f_0)^3 L Q}} \frac{F}{\sqrt{Hz}} \quad (3)$$

where k_B is Boltzmann constant and T is the temperature in degrees Kelvin. From equation 3 we note that the capacitance sensor noise scales inversely with excitation voltage and is proportional to the square root of the temperature, \sqrt{T} . Additionally, a figure-of-merit (FOM) for the measurement is defined as $f_0^3 L Q$. Therefore, the goal is to have a high resonant frequency within the constraints of losses, bandwidth of the amplifiers and demodulation electronics. A capacitance sensing noise limit of $1aF/\sqrt{Hz}$ requires $FOM = 1.34 \times 10^{14}$. Operation at 118 kHz with a 1V excitation requires $LQ = 0.081$. Later calculations will confirm that a $Q \approx 200$ is achievable and yields a required inductance of $L = 0.41$ mH. Introducing a FOM margin of an order of magnitude

yields a desired primary and secondary inductance $L = 4.1$ mH. From equation 1, $C_{eq} = 444$ pF at the 118 kHz excitation frequency and using $C_0 = 1$ pF, results in a tuning capacitance $C_p = 221$ pF. These values are a good starting point for the resonant transformer design.

We designed a compact planar differential transformer using PCB substrates made of ceramic composites^{12,13,14}. The choice of core material is based on low loss and a low temperature coefficient of the complex permeability μ . MnZn or NiZn ferrites are the materials of choice at operating frequencies above 100 kHz. Magnetic cores used with planar devices have a different shape than conventional cores used with helical windings. Compared to a conventional magnetic core of equal core volume, devices built with optimized planar magnetic cores usually exhibit significantly reduced height (low profile), greater surface area, improved heat dissipation capability, greater magnetic cross-section area enabling fewer turns, smaller winding area, and facilitate interleaving and excellent reproducibility enabled by the winding structure. Some of the disadvantages of planar windings are higher intra-winding (same winding, primary or secondary) capacitance and consequently lower self-resonance frequency resulting in a lower Q . This can be mitigated somewhat by staggering the traces on adjacent PCB layers. Ceramic composites have a lower dielectric constant thus resulting in a lower intra-winding capacitance. The figure of merit FOM_c for an ungapped core with initial permeability μ_i and loss factor $\tan\delta$ is given by:

$$FOM_c = \frac{\tan \delta}{\mu_i} \quad (4)$$

Gapped cores with an air gap s that is small compared to the effective magnetic path length l_e in the core have a lower effective permeability μ_e given by:

$$\mu_e = \frac{\mu_i}{1 + \frac{s}{l_e} \mu_i} \quad (5)$$

The effective loss factor is similarly defined as:

$$\tan \delta_e = \frac{\tan \delta}{\mu_i} \mu_e \quad (6)$$

The effective temperature coefficient of the core permeability α_F is also reduced by the ratio of effective and initial permeability:

$$\alpha_E = \frac{\alpha_F}{\mu_i} \mu_e \quad (7)$$

The N48 MnZn ferrite core is a good candidate for our application due to its low temperature coefficient and loss factor²⁶. Commonly available core shapes are Rectangular Modulus (RM), Pot shaped (P), with the RM shape better suited to our application. The TDK N48 datasheet at 120KHz yields $\tan \delta = 0.01$ or $Q = 100$. However, this number is too low for the sensor, and we need to use a gapped core to lower the losses and increase the Q . The N48 MnZn ferrite core with air gap, model B65813A, with $s = 0.13$ mm and $l_e = 44$ mm has an effective permeability $\mu_e = 254$, yielding $\tan \delta_e = 0.0011$ and $Q_{eff} = 905$, a much-improved number.

Finally, the inductance factor A_L is defined as:

$$A_L = \frac{L}{N^2} \quad (8)$$

where N is the number of windings.

The RM10 shaped gapped ferrite core B65813A without a center hole specifies $A_L = 630$ nH. Desired inductance for the bridge primary is 3.9mH and we choose $N = 80$ to get an integer number of turns per layer yielding a 4.03mH winding inductance. The winding Equivalent Series Resistance (ESR) calculated from the equation:

$$R_s = \frac{2\pi f_0 L}{Q} \quad (9)$$

yields $R_s = 3.9$ ohms. R_{pl} , the parallel resistance from core losses, is given by $R_{pl} = R_s \times Q^2$, with $R_{pl} = 2.37$ M Ω . We still need to consider the copper or I^2R losses in the windings/traces from AC resistance (skin effect and proximity effect) and loss enhancement from the self-resonant frequency. The net Q of the transformer will drop, and our goal is to maintain a Q of at least 200 before the amplifier stage.

The effective temperature coefficient of the core α_E is reduced by the ratio of the initial and final permeability to 88 ppb/K. In a differential transformer, where two similar primary windings surround a common core, the temperature coefficient of the core permeability to first order is nulled out. However, a zero initial (DC) imbalance of the inductance between the two primary windings $(\delta L/L)_{DC}$ can fluctuate with temperature and masquerade as a change in capacitance²⁷. An α_E of 88ppb/K makes the contribution negligible. Important properties of the selected core material are tabulated in Table 2.

Table 2. TDK N48 MnZn ferrite core properties

μ_i	$\tan \delta$ (@118kHz)	$\frac{\tan \delta}{\mu_i}$	Q	α_F (ppm/K)	Gapped core μ_{eff}	Q_{eff}	A_L (nH)	α_E (ppb/K)	Core shapes
2300	0.01	4.3×10^{-6}	100	0.8	254	905	630	88	RM, P

II.A. PLANAR WINDING DESIGN

The gapped B65813A core with an airgap of 0.13 mm is specified at an inner and outer diameter of 10.9 (-0.4) mm and 21.2 (+ 0.9) mm, respectively. The maximum mechanical tolerances specified by the manufacturer are in brackets. Therefore, for sizing purposes, the PCB should have a hole of 10.9mm and the outer diameter should be 21.2 mm. Thus, the circular part of the PCB should be sized for $(R_2 - R_1) = 5.15$ mm and the turns will be located on this PCB section.

It is best to use a substrate material with a relatively low dielectric constant to minimize the intra-winding capacitance, with the properties of a few suitable board materials listed in Table 3.

Table 3. Printed circuit board board properties

Parameter	FR4	ISOLA Tachyon 100G	Taconic TSM-29 (PTFE)	Taconic TLX-8 (PTFE)
Dielectric constant ϵ_r	4.40	3.02	2.94	2.55
Dissipation factor D	0.0170	0.0021	0.0015	0.0019
CTE-X	14ppm/K	15 ppm/K	23ppm/K	9ppm/K
CTE-Y	12ppm/K	15 ppm/K	28ppm/K	12ppm/K
CTE-Z	70ppm/K	45 ppm/K	78ppm/K	140ppm/K
Dielectric strength	20MV/m	60MV/m	42MV/m	45MV/m

The TLX series from Taconic²⁸ has the lowest ϵ_r and dissipation factor. The TLY²⁹ series has a lower dielectric constant, but it is harder to procure, laminate and temperature cycle for a multi-layer board design. TLX-8 would be our first choice for the substrate material except it has high z-axis CTE. Conversations with vendors indicate that, considering all requirements, the ISOLA Tachyon 100G material³⁰ is better suited to a multi-layer fabrication with a relatively low z-axis CTE; even though it does not have the lowest ϵ_r . For the current work, FR4 was used due to wide commercial availability, as will be discussed in section III.A.

II.B. TRANSFORMER PRINTED CIRCUIT BOARD DESIGN

We divided the 80 turns around the ferrite core into 5 turns per layer on a 16-layer PCB. The core has a winding depth (defined as height of all windings) of 12.4 mm, inner hole, and outer diameter of 10.9mm and 21.2mm, respectively. We partition the winding depth into 3 planar windings (2 primary and 1 secondary) each 3.1mm thick, leaving us 3.1mm for spacers between windings to reduce the primary-secondary capacitance. Two ring spacers made from low dielectric constant Teflon material with a 1.5mm width and thickness were used as winding separators. The three windings, PCB spacers and the ferrite core were potted together using the low-outgassing adhesive MasterBond EP37-3FLFAO. The stacking order of the windings is primary 1, secondary, primary 2. Interwinding capacitance between the primary and secondary windings is estimated at ~ 2 pF with the temperature coefficient of Teflon. The fringing contribution to the capacitance is negligible for the 1.5 mm spacer. A PCB that can fit around the core selected earlier with a handle-like extension to enable connections to the windings is shown in figure 2. Each layer has 5 turns 0.9 mm wide with a 0.1 mm spacing between them. The turns are slightly staggered by about 0.1mm between the top and bottom layers of each laminate to reduce the inter-winding capacitance. Blind vias across each of the laminates connect the upper set of 5 turns to the inner set on the lower layer of each laminate. Each laminate is connected to its neighboring laminate using a through-hole via located in the flat extender part of the PCB, as shown in Figure 2 to save space for the turns in the circular portion of the PCB that encircles the core. Therefore, for a total of 8 laminates, there are 7 inter-laminate connections and the two terminal connections shown in copper color constitute a 4 mH, 80-turn winding: with the two primary windings and the secondary windings identical. After exchanging the windings in the stack-up, the measured inductances changed by less than 0.02 mH or $<1\%$, thus showing good reproducibility is achieved between all the windings using the printed circuit board technology. These measurements demonstrate the outstanding advantages of planar winding design.

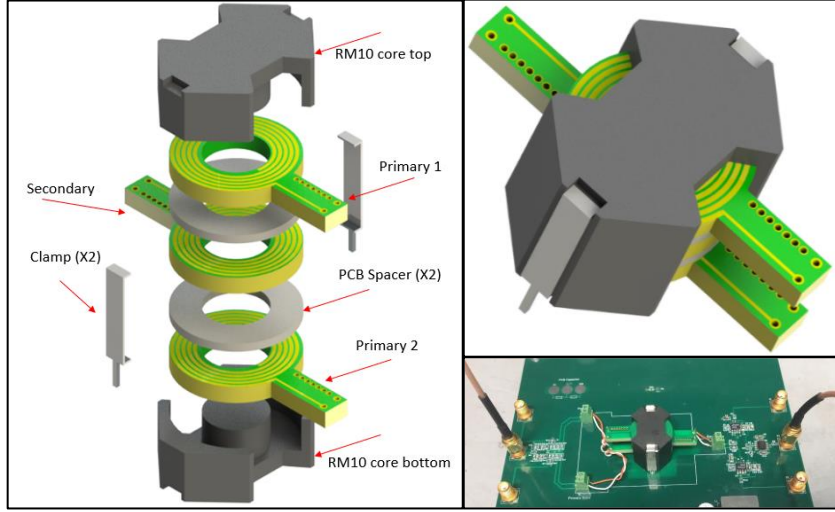


Figure 2. *Left*: Exploded CAD view of the ferrite core, transformer windings, spacers, and clamps. The secondary winding is sandwiched between the two primary windings. The stack-up consists of identical 3.1 mm-thick primary and secondary winding PCBs separated by 1.5 mm spacers that are made from the same PCB material, and potted and clamped around the N48 ferrite core. *Right top*: perspective view of CAD of assembled transformer. *Right bottom*: Photograph of transformer on RCB board.

II.C. LOSS CALCULATIONS

The length of an 80-turn winding in the geometry shown in Figure 2 (left) is about 4032 mm. The average width of each turn is 0.9 mm. For the 35 μm thickness of the PCB traces (1 oz copper), R_{DC} is calculated at 2.15 Ω : using $1.68 \times 10^{-8} \Omega\text{-m}$ for the resistivity of copper. The distributed intra-winding capacitance estimation is based on calculating the total energy associated with the electric field in the 2 layers and extracting the equivalent capacitance. The capacitance of a laminate C_w with n turns on each side can be estimated from the formula³¹:

$$C_w = \frac{(n+1)(2n+1)}{6n} C_0 \quad (10)$$

where $C_0 = \frac{\epsilon_r \epsilon_0}{h_l} A_T$ is the capacitance of a single overlapping turn, h_l is the thickness of the core dielectric material in a single laminate and A_T is the overlapping area of a single turn.

Fringing effects are calculated³² to be $<0.2\%$ for the 100 μm thick laminate and can be neglected. Series connection of m laminates results in a distributed winding capacitance C_d that is given by:

$$C_d = \frac{4(m-1)}{m^2} C_w \quad (11)$$

Therefore, for 5 turns per laminate with a 100 μm laminate core thickness and 8 laminates per winding, the distributed intra-winding capacitance C_d is estimated at ~ 15 pF for a dielectric material with $\epsilon_r = 2.55$, like the Taconic TLX-8 (PTFE). The self-resonant frequency of the winding can now be calculated from:

$$f_{sr} = \frac{1}{2\pi\sqrt{LC_d}} \quad (12)$$

and yields 650 kHz. The apparent Q at the bridge drive frequency of $f_0 = 118$ kHz will drop to $0.96Q$, a 4% reduction. Equivalent additional resistance R_{sr} from the coil self-resonance is:

$$R_{sr} = 2 * R_{dc} * \left(\frac{f_0}{f_{sr}}\right)^2 \quad (13)$$

which calculates to 0.15 Ω . Dielectric losses due to the lossy substrate are estimated at $R_d = 0.12 \Omega$ using the formula:

$$R_d = \tan\delta_d * 2\pi f_0 L * \left(\frac{f_0}{f_{sr}}\right)^2 \quad (14)$$

Finally, AC losses from the skin and proximity effects can be estimated. At 118 kHz, copper with a resistivity of $\rho = 1.68 \times 10^{-8} \Omega\text{-m}$ has a skin depth $\delta_s = 188 \mu\text{m}$. For 1 oz copper the trace thickness is the same for each of the layers: $h = 35 \mu\text{m}$. The parameter for estimating eddy and proximity effect losses is $\xi = h / \delta_s$. For 1 oz copper $\xi = 0.186$. The expression for AC resistance of the m^{th} layer that incorporates the skin and proximity effects can be written as^{31,33}:

$$\frac{R_{ac,m}}{R_{dc,m}} = \frac{\xi}{2} \left[\frac{\sinh \xi + \sin \xi}{\cosh \xi - \cos \xi} + (2q - 1)^2 \frac{\sinh \xi - \sin \xi}{\cosh \xi + \cos \xi} \right] \quad (15)$$

where q is defined as:

$$q = \frac{F(h)}{F(h) - F(0)} \quad (16)$$

and $F(h)$ and $F(0)$ are the MagnetoMotive Forces (MMFs) at the top and bottom of a layer. For a layer count of 16, and using the skin depth of copper calculated earlier, $R_{ac}/R_{dc} = 1.03$ at 118 kHz. Therefore, the loss due to the skin and proximity effects is modelled as an extra resistance $R_{ac} = 0.07 \Omega$. Adding all the losses to get an equivalent loss resistance:

$$R_{tot} = R_{dc} + R_{ac} + R_{sr} + R_d \quad (17)$$

and yields $R_{tot} = 2.5 \Omega$. Adding a 50% error margin, we use $R_{tot} = 3.75 \Omega$ for the Q calculations.

The quality factor of the winding recalculates to 810 and the equivalent parallel resistance $R_{p2} = 2.46 \text{ M}\Omega$. Now place this in parallel with the equivalent parallel resistance $R_{p1} = 2.37 \text{ M}\Omega$ from core losses as calculated earlier. Therefore $R_B = 1.2 \text{ M}\Omega$ and this is the effective resistance of the bridge from the core, including copper and dielectric losses. The net effective Q of the bridge with all losses factored is calculated at 395 and we are almost a factor of 2 better than the original design goal. The tuning capacitance required to assure resonant operation at the bridge excitation frequency calculates to 436 pF from equation 1. Since $C_{eq} = 2(C_0 + C_p)$, and accounting for an intra-winding capacitance of 15 pF, the required tuning capacitance $C_p = 202 \text{ pF}$. This can be achieved with a 180 pF capacitor in parallel with a 22 pF capacitor with good temperature stability (ceramic, NP0 type). The temperature coefficient of the intra-winding capacitance is to first order the z-axis CTE of the substrate.

Assuming we use a Taconic TLX-8 substrate, the z-axis temperature coefficient is 45 ppm/K while the temperature coefficient of a high-quality ceramic NP0 capacitor is typically 10 ppm/K. The composite temperature coefficient of the tuning capacitance can be estimated at 20 ppm/K. The resulting shift in the resonant frequency would be 10 ppm/K. Therefore, the detuning from resonance of the 120 kHz excitation frequency would be 1.2 Hz/K. The secondary signal appears to be slightly reactive with a phase of about half a degree with respect to the excitation signal at 118 kHz. The output amplitude and the capacitance measurement have a temperature coefficient of 50 ppm and 0.20 aF/K, respectively. The thermal noise of the bridge impedance R_B at resonance drives the system measurement noise to first order. Substituting the value of L and Q into equation 6 for the capacitance readout noise yields $S_c^{1/2} = 0.22 \text{ aF}/\sqrt{\text{Hz}}$. The amplifiers that follow the

transformer add noise to the measurement, but as calculated later in the paper, their contribution should be much lower than the bridge thermal noise.

III. RESONANT CAPACITANCE BRIDGE CIRCUIT

The schematic of the measurement system is shown in Figure 3. The differential transformer secondary is connected to a pair of transimpedance amplifier (TIA) stages with a feedback network Z_{FB} to convert the secondary currents into proportional voltages. Circuit analysis¹⁰ yields the transfer function at resonance as

$$\frac{u_o}{u_i} = k \frac{2\Delta C}{C_{FB}} G_{diff} G_{ext} \quad (18)$$

where ΔC is the differential capacitance, $C_{FB} = 2.2\text{pF}$ is the feedback capacitance of the TIA stages and $k = 0.95$ is the transformer coupling factor. $G_{diff} = 10$ is the gain of the capacitively coupled differential amplifier stage that converts the TIA outputs to a single-ended output for transfer function and noise measurements. An external $G_{ext} = 10$ stage using a quiet LT1028 operational amplifier was connected to get the bridge output well above the instrument noise floor.

The readout sensitivity measures 86.4 mV/fF at 1 V excitation. The TIA noise is calculated at $22.6\text{ nV}/\sqrt{\text{Hz}}$ from the noise gain amplification of the AD8510 JFET operational amplifiers voltage noise e_n , $2.6\text{ nV}/\sqrt{\text{Hz}}$ from the operational amplifier current noise i_n flowing through the feedback impedance and $34.6\text{ nV}/\sqrt{\text{Hz}}$ from the Johnson noise contribution of the real part of the feedback impedance at resonance. The total TIA noise is calculated at $41.4\text{ nV}/\sqrt{\text{Hz}}$ and verified using LTSpice simulation code. The transformer thermal noise at the output of the TIA stage is calculated at $134\text{ nV}/\sqrt{\text{Hz}}$ and is clearly the dominant source of noise. Therefore, the total noise at the output of the TIA + differential amplifier + external gain stage is calculated at $14\text{ }\mu\text{V}/\sqrt{\text{Hz}}$. This translates into a capacitance noise floor of $0.22\text{ aF}/\sqrt{\text{Hz}}$ after factoring in the $\sqrt{2}$ demodulation penalty as discussed earlier.

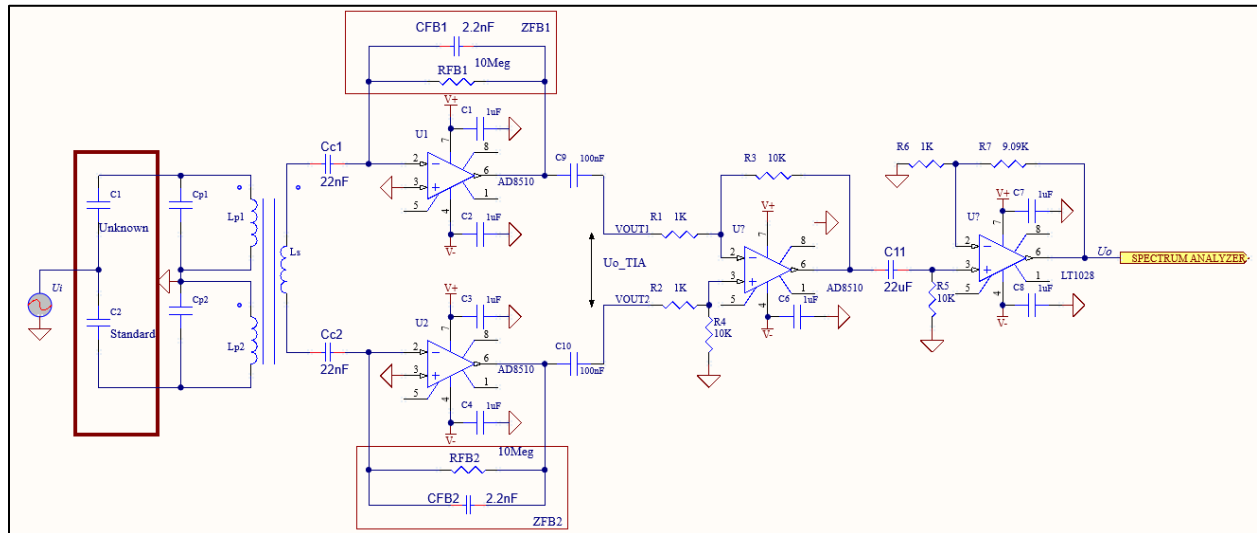


Figure 3. Schematic of the symmetrical differential transimpedance amplifier stage with a single gain setting component C_{FB} per operational amplifier. C_C couples the transformer to the operational amplifier and R_{FB} provides a path for the operational amplifier DC bias current. Z_{FB1} and Z_{FB2} are the complex impedances of the feedback networks. A differential 10X stage followed by an external 10X amplifier is connected to a spectrum analyzer for capacitance and noise floor measurements.

III.A. TRANSFORMER MEASUREMENTS

As mentioned above, due to availability constraints, the planar primary and secondary coils were fabricated on a FR4 substrate, rather than the preferred Taconic TLX-8 (PTFE), thus resulting in an increased dielectric constant ϵ_r and dissipation factor D . The FR4 laminates-based transformer windings had good Q numbers, and the final measurements were better than 0.4 aF/ $\sqrt{\text{Hz}}$ capacitance noise floor. The FR4 PCB windings were characterized using an RLC meter and the measurements are shown in Table 4. The coils were stacked as shown in Figure 2 (top right) and the coil resistance, inductance and Q were measured. The secondary coil had a 10% lower measured inductance than expected due to its central position in the coil stack farthest from the ferrite core base and top. One core, designated as CORE#1 was used for all measurements presented in sections III.A, III.B, and III.C. Results in sections III.D and III.E were obtained with both CORE#1 and CORE#2.

The leakage inductance of all three planar coils were measured by shorting the other two windings and measuring coil inductance of the single winding. The transformer coupling factor k can be calculated from these inductance measurements. All measurements were performed at the standard RLC meter measurement frequency of 100 kHz. Interchanging individual coils did not affect the measurements indicating excellent reproducibility between the planar windings.

C_{eq} , the capacitance required to resonate with the measured primary inductance at the bridge excitation frequency, is calculated at 690 pF by using equation 1. The tuning capacitances C_{p1} , and C_{p2} required in the measurement circuit calculate to 324pf, after allowing for the calculated winding capacitance C_w . These were synthesized using a 300 pf and a 24 pf C0G/NP0 ceramic capacitors in parallel. The bridge resonant frequency of 117.75 kHz was measured by driving the bridge with a function generator and noting the frequency at peak output voltage of the transimpedance stage. By adjusting the tuning capacitors, the resonance frequency can be tuned to any desired value in the range 118 ± 5 kHz without changing the RCB performance.

Table 4. Planar transformer coil measurements @ 100KHz

Winding	L (mH)	$L_{\text{leakage}}(\mu\text{H})$	k	DCR(Ω)	ESR(Ω)	C_w (pf) calculated	Q
Primary 1	2.55	264.9	0.95	2.61	16.08	21pf	98.5
Primary 2	2.56	263.2	0.95	2.63	16.3	21pf	97.4
Secondary	2.3	115.5	0.974	2.6	18	21pf	79.2

III.B. CAPACITANCE MEASUREMENTS

The capacitance bridge was excited with a 100 mV_{rms} sinewave at 117.75 kHz using an HP 8648A signal generator. A differential capacitance was introduced between C_1 and C_2 and carefully measured using an Andeen-Hagerling AH 2500A¹⁶ capacitance bridge operating at 1 kHz. The measured capacitances using the AH2500A¹⁶ are 1.6936645 pf and 1.5903912 pf for a $\Delta C = 103.3$ fF. The RCB readout was 11.76 dBm as shown in Figure 4. This power level is equivalent to 0.866 V in a 50 Ω system. Using 8.64 mV/fF as the conversion factor at 0.1 V excitation yields a differential capacitance of 100 fF. The difference between the RCB and the AH2500A¹⁶ bridge measurements is $\sim 1.5\%$. We note that the AH2500A measurement frequency is 1 kHz while the resonant bridge operates at 117.75 kHz which explains the difference between the two measurements.



Figure 4. The RCB output for a frequency scan across the bridge resonant frequency with a $100\text{mV}_{\text{rms}}$ excitation input and $\sim 100\text{ fF}$ differential capacitance. Scan: 117 kHz to 120 kHz (0.3 kHz/division)

III.C. NOISE FLOOR MEASUREMENTS

The excitation input to the bridge was terminated to ground with a 50ohm load. A Rohde & Schwarz (R&S) model FSV40-N³⁴ spectrum analyzer was connected to the output of the RCB for noise floor measurements as shown in Figure 5. The noise floor at 117.75 kHz was measured at -60.56 dBm at a resolution bandwidth (RBW) of 100Hz with a 100 average count as shown in Figure 5. Using the 86.4 mV/fF conversion factor and dividing by the square root of the RBW yields a capacitance noise floor of $0.23\text{ aF}/\sqrt{\text{Hz}}$. Accounting for the $\sqrt{2}$ noise penalty from the demodulation process yields a sensor sensitivity of about $0.33\text{ aF}/\sqrt{\text{Hz}}$. The excitation frequency corresponds to a noise minimum in the output, a compelling demonstration of the benefits of resonant operation. Note that, while the Q of the transformer is ≈ 100 , components of the RCB including the FET amplifiers (with a bandwidth of $\approx 8\text{MHz}$), the feedback resistors, and others introduce losses that drop the overall Q of the circuit by a factor of approximately 2.

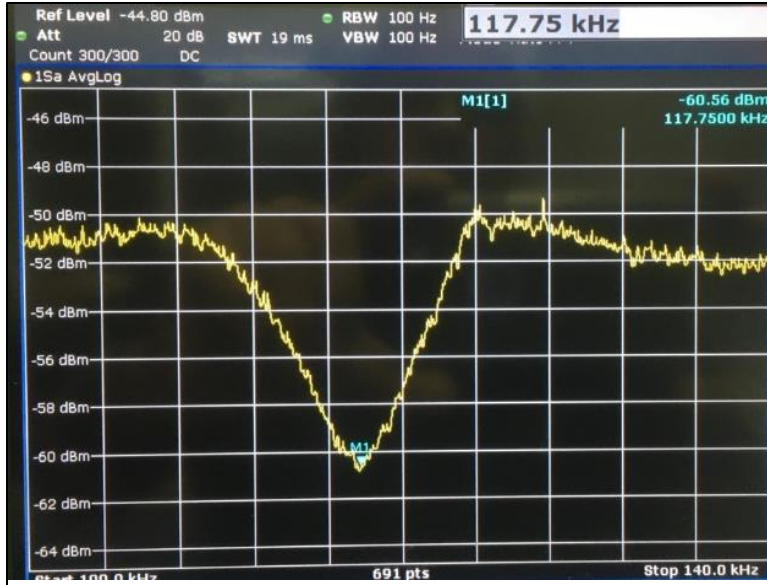


Figure 5. Noise floor measurements of the RCB. The marker (blue M1) is located at the bridge resonance frequency, the noise minimum of the resonant system. Scan: 100 kHz to 140 kHz (4 kHz/division).

III.D LONG TERM NOISE FLOOR AND STABILITY

The long-term noise at the bridge resonant frequency was measured for both cores using the R&S spectrum analyzer for both cores. The noise floor after a continuous quiet measurement period was recorded and the resulting stability performance was excellent, as shown in Figure 6; with a noise floor of -60.68 ± 0.24 dBm for CORE#1 and -58.50 ± 0.20 dBm for CORE#2, at 117.75 kHz, over a 28-hour measurement period. This corresponds to a capacitance measurement averaged sensitivity of 0.36 ± 0.01 aF/ $\sqrt{\text{Hz}}$ for CORE#1 and 0.46 ± 0.01 aF/ $\sqrt{\text{Hz}}$ for CORE#2 at a Fourier frequency of 10 μHz . These measurements demonstrate the long term stability of the RCB and provide a first order estimate of the reproducibility of the system. As a comparison benchmark, the 12 RCBs of the LISA Pathfinder mission showed a variation between 0.4 aF/ $\sqrt{\text{Hz}}$ and 1.1 aF/ $\sqrt{\text{Hz}}$, see reference 10. Our setup is in an open lab and is therefore affected by the daily thermal cycle. Improvements in the long-term stability of the system can be achieved with a suitable thermal enclosure for the bridge transformer and front-end electronics.

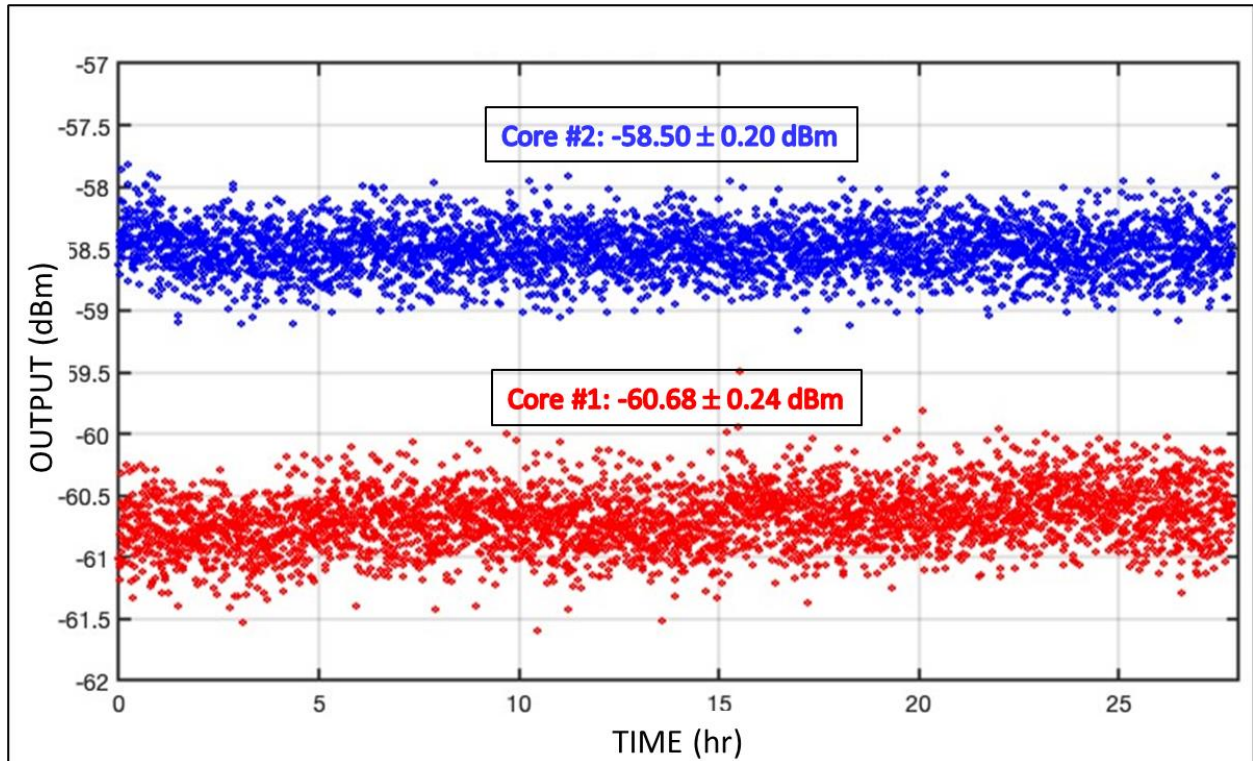


Figure 6. Long-term noise floor measurements of the RCB for CORE#1 (red) and CORE#2 (blue)), with a 300-sweep average over a 28-hour continuous measurement period.

III.E CRYOGENIC MEASUREMENTS

The noise floor of the instrument is essentially set by the thermal noise of the transformer as discussed earlier in the paper and scales as the square root of temperature. This assumes that there are no significant changes in the physical and electrical properties of the components. The measurement sensitivity also scales as the square root of LQ as per equation 3. We expect the bridge Q to drop at lower temperatures due to the negative temperature coefficient of the core permeability. In order to improve the sensitivity of the bridge, the transformer was cooled to 120 K using liquid Nitrogen (LN2) as the coolant in a dewar flask. The transformer and NP0 tuning capacitors were installed on a circuit board that was inserted into the dewar containing about 1 liter of LN2. The transimpedance amplifiers and subsequent amplifier stages were on a separate circuit board outside the dewar in ambient air. The transformer secondary winding was connected to the amplifiers outside the dewar using a twinax with the shield driven at the electronic ground of the amplifier system to minimize noise pickup in the laboratory.

Figure 7 shows the noise floor of the instrument with CORE#1 at room temperature and at 120 K after retuning the resonant frequency to its room temperature value of ~ 118 KHz. The noise reduction is ~ 4 dB which corresponds to a $\sim 37.5\%$ improvement in capacitance measurement sensitivity. Thermal noise scales as the square root of the temperature, resulting in an expected 35% improvement in sensitivity between 120 K and 300 K; close to the measured 37.5%. Bridge Q at room temperature is measured at ~ 30 while it drops to ~ 19 at 120K. The reduction in Q is a consequence of the negative temperature coefficient of the permeability and it can be estimated at 0.24%/K.

Extrapolating the thermal noise and lower ohmic losses to 3 K yields a sensitivity of $0.03 \text{ aF}/\sqrt{\text{Hz}}$, which might however require a chemical redesign of the ferrite core³⁵. This is an encouraging prediction and in principle we could measure an energy change of 0.2 eV.

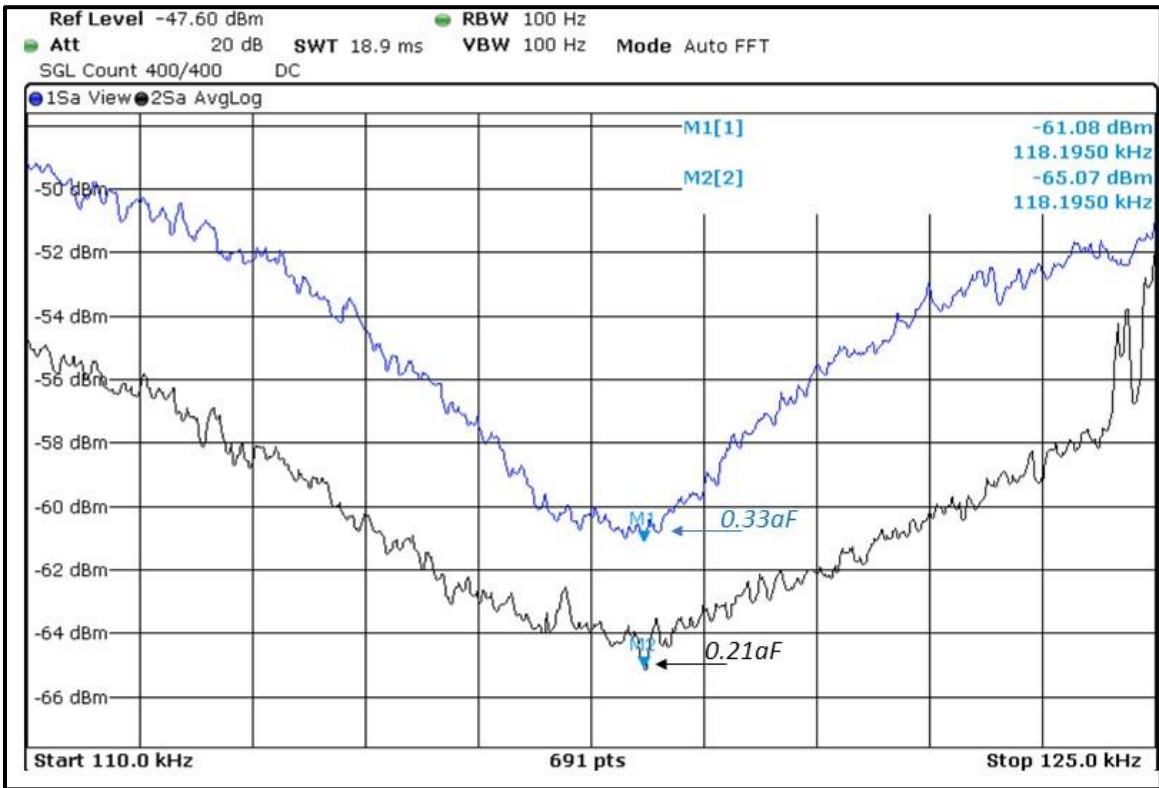


Figure 7 Noise floor measurements for CORE#1 at room temperature (blue trace) and 120 K (black trace). The minima correspond to a detection sensitivity of $0.33 \text{ aF}/\sqrt{\text{Hz}}$ and $0.21 \text{ aF}/\sqrt{\text{Hz}}$, at room temperature and 120K, respectively. Scan: 110 kHz to 125 kHz (1.5 kHz/division)

Measurements with CORE#2 yielded the results shown in Figure 8 for 293 K, 235 K, 142 K and 125 K. Stabilization times were one hour for 293 K and 125 K, ensuring thermal equilibrium of the system, and resulting in a noise floor improvement from $0.42 \text{ aF}/\sqrt{\text{Hz}}$ to $0.34 \text{ aF}/\sqrt{\text{Hz}}$, an increase in Q from about 24 to 30 and a shift in resonant frequency from about 120 kHz to 132 kHz. For a real signal on the bridge, the two transformer windings will undergo the same change in inductance and the differential signal, to first order, will stay unchanged. However, assuming the NPO ceramic capacitors have a relatively low temperature coefficient, the resonant frequency will increase at lower temperatures, given that the permeability (and in turn the inductance) decreases as we lower the temperature. Therefore, the RCB will need to be re-tuned to its new resonance frequency in order to minimize the noise floor. From the data in Figure 8 we estimate the temperature coefficient of the resonant frequency to be about $60 \text{ Hz}/\text{K}$. The measurements at 235 K and 142 K were performed during active cooldown, and, while demonstrating the trends for the noise floor, the Q , and the resonant frequency, do not reliably represent the equilibrium parameters of the RCB at these temperatures.

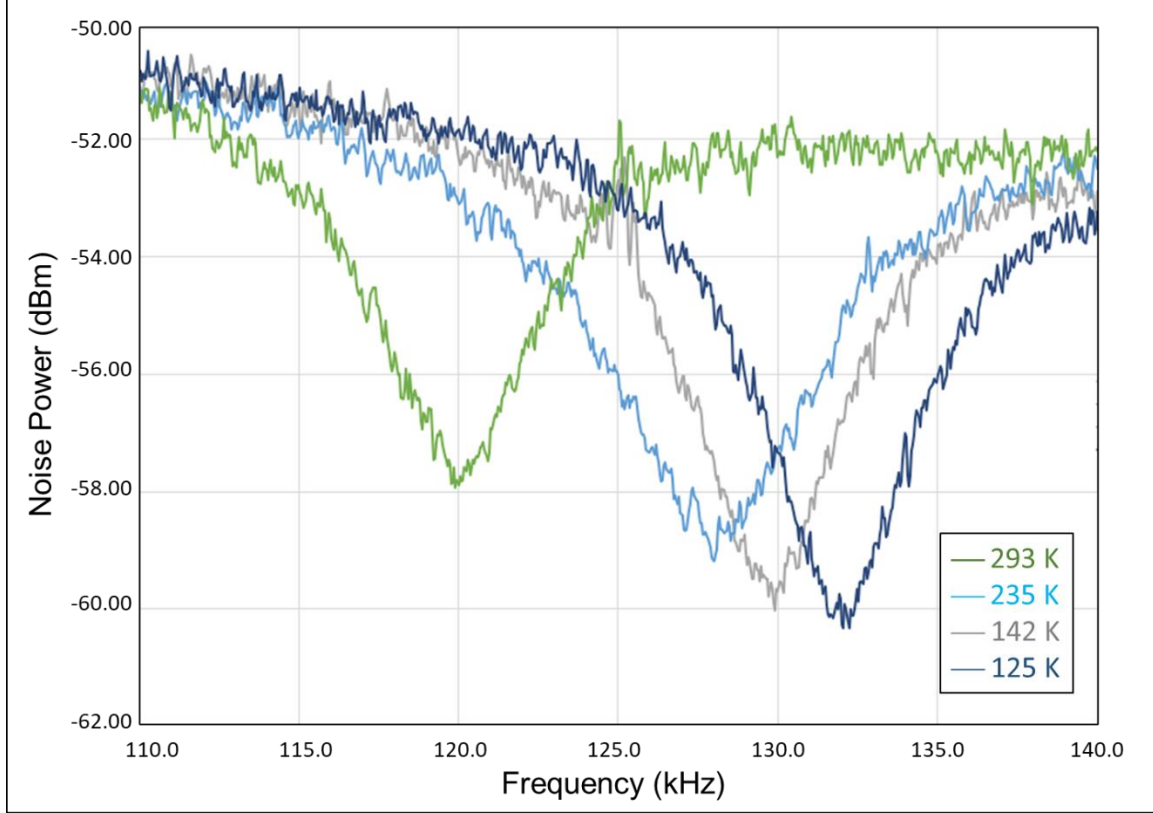


Figure 8. Noise floor measurements for CORE#2 at room temperature (green trace), 235 K (light blue trace), 142 K (gray trace) and 125 K (dark blue trace). The minima correspond to a detection sensitivity of 0.42 aF/ $\sqrt{\text{Hz}}$ and 0.34 aF/ $\sqrt{\text{Hz}}$, at 293 K and 125K, respectively.

IV. CONCLUSIONS

We have designed, modelled, and fabricated the front-end of a precision capacitance bridge with a measured long-term average sensitivity of 0.36 ± 0.01 aF/ $\sqrt{\text{Hz}}$. The differential transformer at the heart of the resonant capacitance bridge was fabricated using planar windings on a FR4 PCB and ferrite cores with excellent repeatability, as demonstrated with a second core, and a low temperature coefficient of about 60 Hz/K. Further improvements in the transformer Q and overall capacitance sensitivity can be achieved by using lower ϵ_r and lower loss ceramic substrates for the windings. Implementation of a synchronous demodulator to extract the DC capacitance signal with the inherent noise penalty of $\sqrt{2}$ yields a sensitivity of 0.36 aF/ $\sqrt{\text{Hz}}$. The bridge easily meets the demanding requirements of a position sensor for a drag-free gravitational reference sensor⁹. Cooling of the transformer to 120 K using LN2 improved the bridge sensitivity by 37.5% yielding a detection threshold of 0.21 aF/ $\sqrt{\text{Hz}}$.

ACKNOWLEDGEMENTS

SN&N Electronics acknowledges funding from the Changchun Institute of Optics, Fine Mechanics and Physics (CIOMP) for the feasibility study and subsequent fabrication and test of the precision capacitance bridge at room temperature.

References

- ¹ Y. Ye *et al.*, "A Review on Applications of Capacitive Displacement Sensing for Capacitive Proximity Sensor," [IEEE Access](#) **8**, 45325 (2020)
- ² S. Lányi and M. Hruskovic, "The resolution limit of scanning capacitance microscopes" [J. Phys. D: Appl. Phys.](#) **36**, 598 (2003)
- ³ W J Bencze *et al.*, "The Gravity Probe B electrostatic gyroscope suspension system (GSS)" [Class. Quantum Grav.](#) **32**, 224005 (2015)
- ⁴ J. Bergé, P. Touboul, and M. Rodrigues, "Status of MICROSCOPE, a mission to test the Equivalence Principle in space" [J. Phys. Conf. Ser.](#) **610**, 012009 (2015)
- ⁵ T. J. Sumner *et al.*, "STEP (satellite test of the equivalence principle)", [Adv. Space Res.](#) **39**, 254 (2007)
- ⁶ K. Danzmann and the LISA study team, "LISA: laser interferometer space antenna for gravitational wave measurements" [Class. Quantum Grav.](#) **13**, A247 (1996)
- ⁷ Z. Luo *et al.*, "The Taiji program: A concise overview" [Prog. Theor. Exp. Phys.](#) **5**, 05A108 (2021)
- ⁸ J. Luo *et al.*, "TianQin: a space-borne gravitational wave detector" [Class. Quantum Grav.](#) **33**, 035010 (2016)
- ⁹ O. Jennrich, "LISA technology and instrumentation" [Class. Quantum Grav.](#) **26**, 153001 (2009)
- ¹⁰ M. Armano *et al.*, "Capacitive sensing of test mass motion with nanometer precision over millimeter-wide sensing gaps for space-borne gravitational reference sensors" [Phys. Rev. D](#), **96**, 062004 (2017).
- ¹¹ [SN&N Electronics](#), 1846 Stone Avenue, San Jose, CA 95125, United States
- ¹² S. Saraf, S. Buchman, J. Lipa, S. Wang, "A Conceptual Feasibility Study for a High Precision Resonant Capacitance Bridge with Applications in Gravitational Wave Detectors", SN&N technical report, October 10 (2020)
- ¹³ S. Saraf, "Design, Development and Fabrication of a High Precision Resonant Capacitance Bridge with Applications in Gravitational Wave Detectors – Interim Report" SN&N technical report, July 19 (2021)
- ¹⁴ S. Saraf, "Design, Development and Fabrication of a High Precision Resonant Capacitance Bridge with Applications in Gravitational Wave Detectors – Final Report" SN&N technical report, September 9, (2022)
- ¹⁵ Y. Sui *et al.*, "Analysis of a Capacitive Sensing Circuit and Sensitive Structure Based on a Low-Temperature-Drift Planar Transformer" [Sensors](#) **22(23)**, 9284 (2022)
- ¹⁶ [Andeen-Hagerling](#), 31200 Bainbridge Road, Cleveland, Ohio 44139, United States
- ¹⁷ [GRACE](#), Gravity Recovery and Climate Experiment (2002-2018)
- ¹⁸ [GRACE-FO](#), Gravity Recovery and Climate Experiment Follow-On, (2018-continuing)
- ¹⁹ [GOCE](#), Gravity field and steady-state Ocean Circulation Explorer (2009-2013)
- ²⁰ [MICROSCOPE](#), Micro-Satellite à traînée Compensée pour l'Observation du Principe d'Equivalence (2016-2018)
- ²¹ [LISA Pathfinder](#), Laser Interferometer Space Antenna Pathfinder Mission, (2015-2017)
- ²² P. Touboul, B. Foulon, M. Rodrigues, J.P. Marque, "In orbit nano-g measurements, lessons for future space missions" [Aerospace Science and Technology](#), **8(5)**, 431 (2004)
- ²³ P. Touboul *et al.*, "Gravitation and geodesy with inertial sensors, from ground to space" [Aerospace Lab](#), **12**, 1-16 (2017)

-
- ²⁴ M. Hu *et. al.*, “Resonant frequency detection and adjustment method for a capacitive transducer with differential transformer bridge” [Rev. Sci. Instrum. **85**, 055001](#) (2014)
- ²⁵ Y. Xie *et. al.*, “Modeling and Analysis of the Noise Performance of the Capacitive Sensing Circuit with a Differential Transformer” *Micromachines* (Basel), **10(5)**, 325 (2019)
- ²⁶ TDK Electronics, [SIFERRIT material N48](#)
- ²⁷ Davor Mance, “Development of Electronic System for Sensing and Actuation of Test Mass of the Inertial Sensor LISA” [PhD thesis, University of Split](#) (2012)
- ²⁸ Taconic, [TLX Series High Volume Fiberglass Reinforced Microwave Substrate](#).
- ²⁹ Taconic, [TLY Family of Low Loss Laminates](#).
- ³⁰ ISOLA, [Tachyon 100G Processing Guide](#).
- ³¹ Z. Ouyang, O. C. Thomsen and M. A. E. Andersen, “Optimal Design and Tradeoff Analysis of Planar Transformer in High-Power DC–DC Converters” [IEEE T. Ind. Electron., **59\(7\)**, 2800](#) (2012).
- ³² X. Chen, *et. al.*, “Fringing Effect Analysis of Parallel Plate Capacitors for Capacitive Power Transfer Application” [Proc. 4th IEEE International Future Energy Electronics Conference IEEE](#) (2019)
- ³³ P. L. Dowell, “Effects of eddy currents in transformer windings” [Proc. Inst. Elect. Eng., **113\(8\)**, 1387](#) (1966)
- ³⁴ [Rohde & Schwarz FSV40-N 40GHz](#) Signal Spectrum Analyzer
- ³⁵ G.F. Dionne, “Properties of ferrites at low temperatures (invited)” [J. Appl. Phys., **81**, 5064](#) (1997)